International Journal of Multiphase Flow 36 (2010) 599–607

Contents lists available at ScienceDirect

International Journal of Multiphase Flow

journal homepage: www.elsevier.com/locate/ijmulflow

Multiphase flow in the vascular system of wood: From microscopic exploration to 3-D Lattice Boltzmann experiments

X. Frank [a,*], G. Almeida [b], P. Perré [c]

[a] INRA, UMR 1092 LERFOB, F-54042 Nancy cedex, France
[b] USP, ESALQ (Luiz de Queiroz College of Agriculture), Brazil
[c] AgroParisTech, UMR 1092 LERFOB, ENGREF 14, rue Girardet F-54042 Nancy cedex, France

ARTICLE INFO

Article history:
Received 16 February 2010
Received in revised form 22 April 2010
Accepted 24 April 2010
Available online 7 May 2010

Keywords:
Multiphase
Wood
3D modelling
Image processing
Lattice Boltzmann
Vascular
Morphology

ABSTRACT

This paper provides insights into liquid free water dynamics in wood vessels based on Lattice Boltzmann experiments. The anatomy of real wood samples was reconstructed from systematic 3-D analyses of the vessel contours derived from successive microscopic images. This virtual vascular system was then used to supply fluid–solid boundary conditions to a two-phase Lattice Boltzmann scheme and investigate capillary invasion of this hydrophilic porous medium. Behavior of the liquid phase was strongly dependent on anatomical features, especially vessel bifurcations and reconnections. Various parameters were examined in numerical experiments with ideal vessel bifurcations, to clarify our interpretation of these features.

1. Introduction

The xylem (wood) in trees is formed by the cambium. The role of this meristem is to enlarge each stem produced by the apical meristems. In living trees, the formation of wood provides mechanical support, allows reorientation and provides a vascular system, this latter differing between softwoods and hardwoods. In softwood, the vascular system consists of tracheids which are a few millimeters long and connected together by bordered pits. These pits serve as valves which limit the extension of undesired cavitation in the sap column. More precisely, the tracheids formed during spring have thin cell walls, wide radial diameters and hence a large lumen, and are more specifically involved in sap conduction. In hardwoods, the vascular system consists of tube-like vessels, varying in length from a few centimeters to several meters and formed by lines of cells known as vessel elements (Zimmermann, 1983). The ends of these vessel elements are perforated. Matching perforations between adjacent vessel elements provide an open passage for the upward movement of raw sap in the tree stem (Panshin and de Zeeuw, 1980). Hardwoods in which the vessels are fairly uniform in size and relatively evenly distributed throughout the growth ring are described as diffuse-porous woods. Vessels can account for 7–50% of the wood volume, depending on the species. In most diffuse-porous hardwoods of temperate zones, the vessel diameter varies from 20 μm to 100 μm. Air–water flow is crucial in the living tree, as bubbles trapped within the vascular system will have dramatic consequences on permeability and the efficiency of sap transport from roots to leaves. Wood is a hygroscopic porous medium, which means that within it water can exist in three different forms: bound water in the cell walls, free water and water vapor in the cell lumens. However, the diffusion of bound water occurs so slowly (Siau, 1984; Agoua et al., 2001) that fluid migration in wood can be considered as limited to mono- or multiphase flow in the vascular system.

As the anatomy of wood is highly complex, the fluid migration properties (permeability, capillary pressure, relative permeability) cannot be readily deduced from a simple geometrical representation of the vascular system. The situation is even more complex in softwoods, due to the presence of bordered pits between the tracheids. Although interesting models are available in the literature, they usually require considerable assumptions in order to be operational (Comstock, 1970; Perré and Turner, 2001; Aumann and Ford, 2002). The typical dual-scale mechanisms of fluid flow occurring in softwoods (tracheids and bordered pits) explains why some works have focused solely on fluid flow inside a single bordered pit (Hacke et al., 2004; Valli et al., 2002).

The situation in hardwoods is slightly less complex, due to the presence of specialized cells devoted to sap flow. At first sight, the vascular system of hardwood species can be simply repre-

* Corresponding author.
E-mail address: xfrank@nancy-engref.inra.fr (X. Frank).

0301-9322/$ - see front matter © 2010 Elsevier Ltd. All rights reserved.
doi:10.1016/j.ijmultiphaseflow.2010.04.006

sented as bundles of capillary tubes (Dullien, 1992). However, the measured permeability values are systematically overestimated by the theoretical permeability computed from anatomical images using the Hagen–Poiseuille equation (Zimmermann, 1983; Siau, 1984; Perré and Karimi, 2002). Early investigations by Zimmermann and collaborators (Zimmermann, 1983) in several hardwood species revealed that the vessels did not run in parallel but changed their relative positions in the axial direction. For example, it was shown that individual vessels in maple (*Acer rubrum* L.) and poplar (*Populus* spp.) moved from one vessel cluster to another and never really ended. They also observed that in many cases, two or more vessels could run side by side over considerable distances. This implies that the water conducting units do not have dead ends and water can pass from one vessel system into several others through the pits and perforations. It is thus obvious that the task of water-flow prediction is greatly complicated by the actual pore morphology, namely the tortuosity and change in section shape of the conductive elements, as well as the complex networks resulting from their connection. The situation in which multiphase flow occurs, such as cavitation during the tree's lifespan or in the drying of plant-derived material is even more complicated, requiring evaluation of the propagation dynamics of the air–water meniscus or, at the very least, partition of the liquid phase at equilibrium.

The purpose of this paper was to address different multiphase flow configurations by performing numerical experiments on reconstructed morphologies derived from real wood samples. To achieve this goal, two major difficulties were to be addressed: to reconstruct the wood vessel anatomy in three dimensions from a real wood sample, and to choose and implement a relevant numerical approach.

Impressive tools are currently available in the field of non-destructive testing. Micro-tomographic images obtained with a synchrotron provide a sub-micrometric spatial resolution (down to 200 nm). Such tools have been used to obtain a non-invasive insight into wood structure (Trtik et al., 2007; Steppe et al., 2004). One of the major drawbacks of micro-tomography, however, is the acquisition time. This is why NMR imaging provides a powerful complementary technique for non-invasive investigation of fluid flow dynamics in porous media. Indeed, 3D images of one or more fluid phase(s) are obtained in the case of NMR microscopy with a relatively short acquisition time and a spatial resolution in the order of 10 μm (Tyszka et al., 2005). Such a technique has been used, for example, to assess the behavior of bordered pits in early and late wood of Douglas fir during drainage (Almeida et al., 2008).

However, despite the existence of these amazing tools, to our knowledge a comprehensive approach, from the real sample to the simulation of multiphase flow in 3D morphology, has not yet been proposed for wood. In the present work, a relatively simple, low-cost experimental protocol was applied to reconstruct the 3D morphology of a real wood sample from images collected after successive slicing of a sample with a sledge microtome. This procedure, based on the construction of a 3D grid of points by vectorial image processing, could in future be applied to any data set obtained from NMR imaging or micro-tomography, despite its apparent simplicity.

To complete the sample-to-simulation chain, several conditions need to be satisfied when selecting an appropriate numerical method. Firstly, complex gas–liquid interfacial dynamics, including topological changes such as film ruptures and coalescence, will occur during computation. Secondly, the dynamic behavior of the system will emerge as a result of competition between wetting phenomena and viscous dissipation. In consequence, the fluid–solid interactions need to be correctly implemented, despite the complex geometrical features of wood vessels. Description of the fluid/solid and liquid/vapor interfaces is particularly challenging. Classical paradigms, such as front-tracking schemes (De Sousa et al., 2004), volume-of-fluid models (Štěpánek and Rajniak, 2006) and level-set approaches (Tanguy and Berlemont, 2005), give rise to huge computation loads when the system is large or in the case of complex interfacial geometries. These difficulties might be circumvented by using the seemingly attractive meshless methods (Frank and Perré, 2010). Several alternative numerical methods are available. In off-lattice approaches, the fluid is described through moving point-like elements. For example, in the context of smooth particle hydrodynamics (SPH) (Tartakovsky et al., 2007), the Navier–Stokes equation is solved on Lagrangian particles carrying macroscopic fluid properties and fields. In other numerical methods, macroscopic features can emerge spontaneously from the initial assumptions. Dissipative particle dynamics (DPD), a coarse-grained molecular dynamics approach, is part of this elegant family (Henrich et al., 2007). The Lattice Boltzmann (LB) scheme is another quite recent emergence-based mesoscale numerical tool for fluid flow simulation (Succi, 2001). It can be considered as a special discretization of the well-known Boltzmann's equation, despite its later development, as compared to lattice gas cellular automata (LGCA) (Hardy et al., 1976). The Lattice Boltzmann method has already proved its ability to simulate multiphase flows in porous media (Hatiboglu and Babadagli, 2008). In the present work, the latter was chosen as a satisfactory compromise between the computational work and the size of the computed domain.

2. Wood sample anatomy

2.1. Image acquisition and processing

The study was carried out on a 8-year-old White birch (*Betula verrucosa*). The final cross section dimension of the chosen sample was 3 mm (tangential) × 5 mm (radial) and 20 mm in length (longitudinal). This sample was fixed on a sledge microtome. A modular microscope (Nachet MS 98) equipped with long-focus lens and a digital camera from Basler Vision Technologies (Fig. 1A) was fixed on a support. The microtome chosen for this work had the advantage of vertically displacing the sample between successive cuts, thereby facilitating exploration of the vessel network. A microtome section thickness of 20 μm (along the longitudinal direction) was chosen for sample exploration and a digital image was taken every 40 μm. The images were stored in color (RGB, 8 bits per color) with a spatial resolution of 1388 × 1038. The magnification lens used in this work results in a pixel size of 1.3 μm. In all, 100 images were analyzed resulting in a depth of vascular system exploration of 4000 μm.

The 2-D images were processed with *MeshPore*, a customized software specifically developed for processing vectorial images (Perré, 2005) from a specific data structure. This multi-purpose software is based on the concept of directed line segments and is designed to be able to handle any shape (including closed or open contours), change the number of nodes in each chain, distinguish contour structure and the location of geometrical points, merge or split chains, re-sample a chain to give a more refined or coarser spatial resolution and so on. The basic elements are points and nodes and a contour consists of a chain of nodes, each one pointing towards a specific geometrical point. Each point carries geometrical information whereas each node carries connection information. This results in a very flexible structure, as the point properties are clearly distinct from the node properties. A vessel contour is defined by a chain, which consists of a set of connected nodes. The first node of each chain is stored in a table, which therefore contains the complete chain list for the image. Each node in a chain "knows" the previous node (= 0 for the first node) and the next

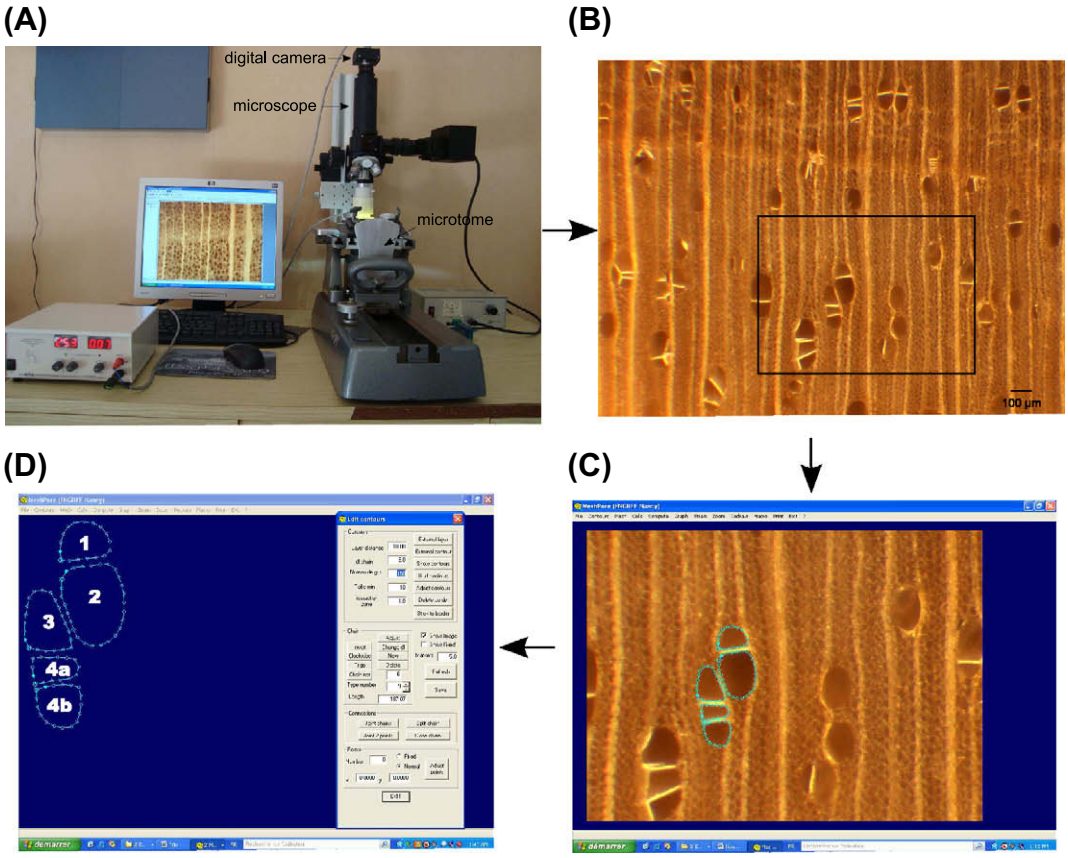

Fig. 1. Image acquisition and treatment. (1A) image acquisition system; (1B) initial image and delimitation of the region of interest (black square); (1C) vessel network demarcation using *MeshPore*; (1D) final 2D image.

node (= 0 for the last node). In the case of a closed chain, the first and last nodes point towards the same point.

As our image collection contained excessive number of vessels, a particular region of interest (ROI) was selected. The macro language available in *MeshPore* allowed easy selection of the same ROI on all images, as well as certain automatic instructions. The main steps of image acquisition and treatment are depicted in Fig. 1.

Due to minute sample movements during successive microtome cuts, a feature has been added to MeshPore to allow for small translations of all chains of an image, in order to align successive planes. Together with the pixel size and the definition of the vessel contour, the global accuracy of our procedure may be estimated at ±2 µm.

2.2. Reconstruction procedure

The LB scheme is based on generation of a 3D lattice with a distinction between pore and solid. As the LB lattice should remain cubic, a certain level of interpolation is required between two successive images, as a function of the desired spatial resolution in the *xy* plane. Note that the vectorial description of the contours provided by *MeshPore* permits a spatial resolution that is independent of the initial bitmap image resolution.

Constructing the true 3D morphology from the collection of n successive planes requires two crucial steps:

1. Finding the connectivities between the contours of successive planes
2. Choosing a method of interpolation between planes to generate a cubic lattice

For this purpose, a 3D version of *MeshPore*, which allows any number of slices to be loaded, has been developed. All the *MeshPore* 2D features were retained for each selected slice, so that the final data set consisted of a collection of planes, each one defined by a collection of chains. The graphical facilities implemented in *MeshPore* 3D used the concept of quaternions to compute the projections.

Numerous criteria can be imagined to find the connectivities between contours. Rather than a criterion based on the common surface area between two contours (Kwon et al., 2003), we chose to use a more demanding criterion i.e., that two contours would be considered as connected if the barycenter of one contour was included in the other. The reciprocity of the criterion is important, namely in the case of bifurcations (one vessel of a plane connected to two vessels of a neighboring plane (upper or lower). We took advantage of our vectorial data representation and made thorough use of integral contours in the data processing. For example, following Stokes's theorem, the barycenter of a closed chain was obtained from the contour integrals:

$$x_{bary} = \frac{1}{S}\oint_C x^2 \cdot dy \tag{1}$$

$$y_{bary} = -\frac{1}{S}\oint_C y^2 \cdot dx \tag{2}$$

Similarly, the Cauchy's residue theorem was used to determine if a specific point was inside a closed contour or not. This criterion was used both to generate the connectivities between contours and to allocate the solid or pore flag to each point of the lattice.

Once all the connectivities had been computed, all the chains were organized into clusters. These clusters (set of connected con-

tours) were built up step by step, until they spread throughout the whole domain.

In order to stay as close as possible to the real vessel morphology, the contours themselves were interpolated before lattice generation. For each couple of connected contours (initial contours) from two successive planes, one contour was built in each interpolation plane by creating a chain with the same number of nodes as the first initial chain. For each node i of the first initial chain, the *best* node of the other chain was chosen to form a generatrix of the vessel pathway. This node was indeed the one whose point was nearest to the plane formed by the two barycenters of the initial chains and the point of node i. The point of the current node of the interpolated chain is simply the intersection of the interpolation plane with this generatrix (Fig. 2).

An example of this interpolation procedure is shown in Fig. 3. This simple configuration depicts the interpolation obtained in two common cases:

- One single contour, slightly deformed and shifted from one plane to the other.
- Two contours connected to a single and larger contour on the upper plane.

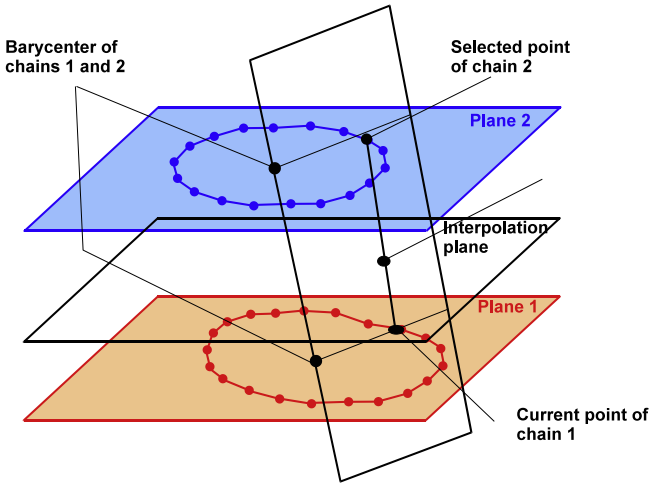

Fig. 2. Strategy used to interpolate 3-D morphology from connected chains of two successive initial planes.

2.3. Example of morphology

A set of four vessels was chosen as case study for the modeling work. The interest of the selected zone was based on two major features:

- The presence of vessel lines of different and variable sections,
- The existence of two bifurcations: one vessel line diverging into two sub-lines, which then merge again into a single vessel

The resulting morphology is depicted in Fig. 4. To ensure easy analysis and discussion of the capillary invasion simulated with this morphology, the vessels were numbered and vessels 4a and 4b indicate the bifurcation of vessel 4.

3. Shan–Chen Lattice Boltzmann approach

In the LB context, the Navier–Stokes equation is not implemented directly, as the fluid is described at the particle kinetics level. Particle presence probability density functions (PPDF) f_i are defined, where $f_i(\vec{r},t)$ is the probability of finding a particle exhibiting velocity $\vec{c}_i$ at point $\vec{r}$ and date t. A lattice is defined from the discrete velocity set $\{\vec{c}_i\}$, where $\vec{c}_i$ velocities are tuned to allow a particle to jump from one node of the lattice to a neighboring node. We chose a three-dimensional lattice which exhibited 19 velocities: the D3Q19 lattice (Table 1).

Fluid density ρ and velocity $\vec{u}$ are provided in a relatively simple way by equations:

$$\rho = \sum_i f_i \tag{3}$$

$$\rho\vec{u} = \sum_i f_i\vec{c}_i \tag{4}$$

The main idea of the Lattice Boltzmann approach is to implement both collisions between particles and free streaming from one collision to the next. To do this we chose the so-called LBGK model in which the f_i fuctions obey a linear approximation of the general lattice Boltzmann equation:

$$f_i(\vec{r}+\delta t\vec{c}_i, t+\delta t) - f_i(\vec{r},t) = -\frac{1}{\tau}\left(f_i - f_i^{eq}\right) \tag{5}$$

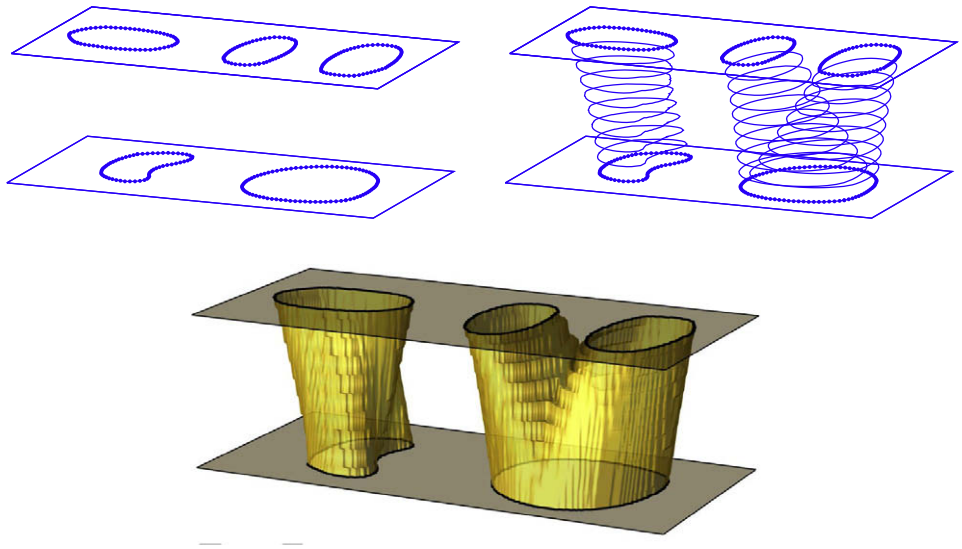

Fig. 3. Example of interpolation between two initial planes: two clusters with one bifurcation (top, left), calculated chains of nine interpolation planes between these two initial planes (top, right) and the 3D morphology obtained after grid generation (bottom).

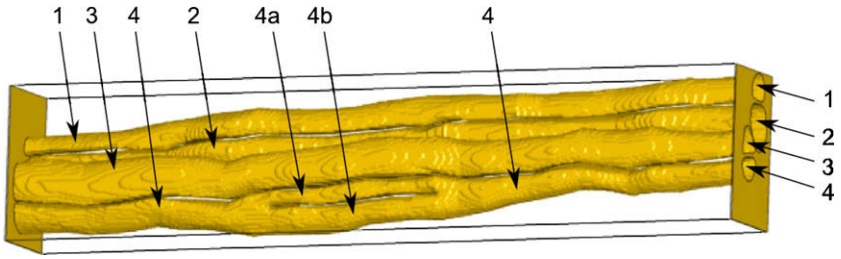

Fig. 4. Re-building of birch anatomy. Numbers are attributed to the vessels. Note that vessel 4 exhibits two bifurcations (divergent and convergent) and the resulting sub-vessels are termed vessel 4a and 4b.

Table 1
The D3Q19 lattice velocities.

i	0	1	2	3	4	5	6	7	8	9	10	11	12	13	14	15	16	17	18
$\vec{c}_i$	0	1	−1	0	0	0	0	1	1	−1	−1	1	1	−1	−1	0	0	0	0
	0	0	0	1	−1	0	0	1	−1	1	−1	0	0	0	0	1	1	−1	−1
	0	0	0	0	0	1	−1	0	0	0	0	1	−1	1	−1	1	−1	1	−1

The left member is implemented through a streaming step and the right member is a relaxation term, where τ is the relaxation time: inter-particle collisions drive f_i towards an equilibrium value f_i^{eq}, which is deduced from macroscopic quantities:

$$\sum_i f_i^{eq} = \rho \tag{6}$$

$$\sum_i f_i^{eq}\vec{c}_i = \rho\vec{u} \tag{7}$$

$$\sum_i f_i^{eq} c_{i\alpha}c_{i\beta} = \rho u_\alpha u_\beta + \rho c_s^2\delta_{\alpha\beta} \tag{8}$$

$$\sum_i f_i^{eq} c_{i\alpha}c_{i\beta}c_{i\gamma} = \rho c_s^2(u_\gamma\delta_{\alpha\beta} + u_\alpha\delta_{\gamma\beta} + u_\beta\delta_{\alpha\gamma}) \tag{9}$$

The value of τ is fixed at $\tau = 1$. Dirichlet boundary conditions were imposed by applying the well-known bounce-back boundary conditions: particles reaching a solid wall are simply reflected in the direction from which they came.

Fluid–fluid interactions are required when performing multiphase flow simulations. Several Lattice Boltzmann models for multiphase flow simulations have been proposed. These include the Gunstensen chromodynamic model (Gunstensen et al., 1991), the free energy-based approach for both liquid/vapor systems (Swift et al., 1995) and binary fluids (Swift et al., 1996), proposed by Swift et *al*, intermolecular interaction-based model of He et al. (1999), the Inamuro approach (Inamuro et al., 2004) and the Lee and Lin scheme (Lee and Lin, 2005). We chose the pseudo-potential approach (Shan and Chen, 1993)for the present work. A modified fluid velocity is computed in which fluid–fluid forces $\vec{F}_{FF}$ occur:

$$\rho\vec{u}' = \rho\vec{u} + \tau\vec{F}_{FF} \tag{10}$$

The modified velocity $\vec{u}'$, provided by Eq. (10), replaces $\vec{u}$ in Eqs. (7)–(9). The interaction forces are deduced from interactions taking place between neighboring particles:

$$\vec{F}_{FF}(\vec{r}) = \psi(\vec{r})\sum_i G_i^{FF}\psi(\vec{r} + \delta t\vec{c}_i) \tag{11}$$

The function $\psi = 1 - e^{-\rho}$ can be interpreted as an effective density. Parameter G_i^{FF} is an interaction parameter, the value of which depends on the direction, following:

$$G_i^{FF} = \begin{cases} 2G^{FF} & \|\vec{c}_i\| = 1 \\ G^{FF} & \|\vec{c}_i\| = \sqrt{2} \end{cases} \tag{12}$$

The scalar parameter G^{FF} must be adjusted to produce a liquid–vapor phase transition.

We implemented this model in a parallel code (FORTRAN and MPI routines) called *FlowPore* (Frank and Perré, 2010). We validated this tool by performing simulations in a cubic box to compute maximum and minimum values ρ_{min} and ρ_{max} of equilibrium ρ fields for various values of G^{FF}.

As can be seen in Fig. 5, our results match well-known results in the literature (Shan and Chen, 1993; Yuan and Schaefer, 2006). To ease the definition of the initial state in practical cases, we tuned the fitting expressions for ρ_{min} and ρ_{max} as a function of G^{FF}. These expressions were provided by equation:

$$\rho_{min/max} = \begin{cases} \rho_c & G^{FF} < G_c^{FF} \\ \rho_c + A(G^{FF} - G_c^{FF})^\alpha & G^{FF} \geqslant G_c^{FF} \end{cases} \tag{13}$$

The critical point is identified as $\rho_c = 0.708$ and $G_c^{FF} = 0.111$ and the parameters are $A = -1.2289$ and $\alpha = 0.234627$ for ρ_{min} and $A = 14.9537$ and $\alpha = 0.68383$ for ρ_{max}.

The value of surface tension σ was deduced from numerical experiments. The numerical setup was defined as follows: a drop was placed at the center of a cubic box, assuming periodic boundary conditions for each direction. Various drop diameters and values of G^{FF} were used. As indicated previously (Shan and Chen, 1993), the pressure difference across a liquid–vapor interface obeys the Laplace law. For a given value of G^{FF}, the value of σ is deduced from the slope of the linear fit of ΔP as a function of $\frac{1}{R}$, where R is the radius of the drop. We tuned following expression for σ as a function of G^{FF}:

$$\sigma = 3.059G^{FF} - 0.368 \tag{14}$$

In the same way, fluid–solid interactions are introduced when solid nodes are present, through a force term $\vec{F}_{FS}$ (Martys and Chen, 1996; Raiskinmäki et al., 2002) which leads to the final expression of the modified velocity:

$$\rho\vec{u}' = \rho\vec{u} + \tau(\vec{F}_{FF} + \vec{F}_{FS}) \tag{15}$$

Vector $\vec{F}_{FS}$ is expressed as:

$$\vec{F}_{FS}(\vec{r}) = \psi(\vec{r})\sum_i G_i^{FS}S(\vec{r} + \delta t\vec{c}_i) \tag{16}$$

The value of parameter $S(\vec{r})$ is 1 if the point $\vec{r}$ is within the solid phase, and 0 otherwise. The fluid–solid interaction parameter G_i^{FS} depends on the direction according to:

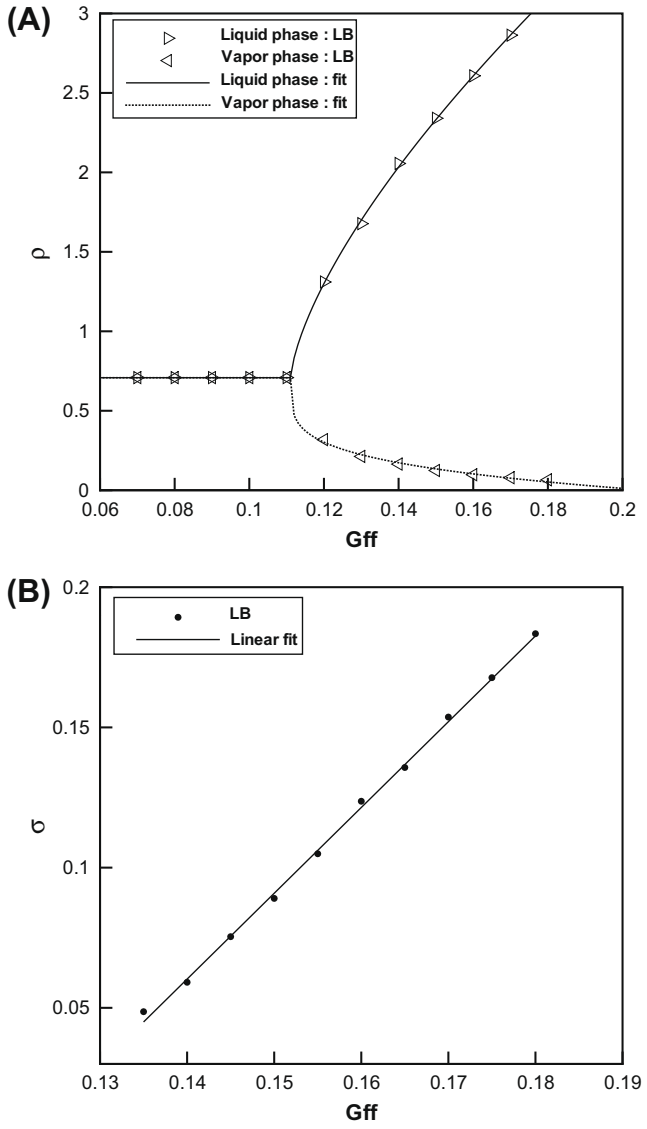

Fig. 5. A: Values of ρ_{min} and ρ_{max} for various values of G^{FF}. Points are from LB simulations and curves are from the expression (13). B: Values of surface tension σ as a function of G^{FF}. Points are from LB simulations and curves are from the expression (14).

$$G_i^{FS} = \begin{cases} 2G^{FS} & \|\vec{c}_i\| = 1 \\ G^{FS} & \|\vec{c}_i\| = \sqrt{2} \end{cases} \tag{17}$$

The value of the static contact angle at the solid–liquid–vapor contact line is dependent both on G^{FF} and G^{FS}, as it emerges from competition between the fluid–solid and fluid–fluid interactions. We estimated the value of the static contact angle by performing systematic 3D simulations for various (G^{FF}, G^{FS}) pairs (Fig. 6). As indicated in the Fig. 6 (inset), we defined a 3D box and placed two solid walls on opposite sides of $\vec{e}_x$ direction, assuming periodic boundary conditions in both other directions $\vec{e}_y$ and $\vec{e}_z$. A liquid layer is placed between two $y = cste$ planes, and the simulation is carried out until equilibrium is reached. The value of the contact angle can then be evaluated.

As can be seen in Fig. 6, a wide range of θ_c values is available. However, both G^{FS} and G^{FF} have to be tuned if a fixed value of θ_c is required.

Despite their extreme simplicity, pseudo-potential-based models have been successfully applied to numerous concrete cases, especially multiphase flow in porous media (Vogel et al., 2005; Sukop and Or, 2004; Sukop et al., 2008; Hatiboglu and Babadagli, 2008) and microfluidics (Yu et al., 2007; Sbragaglia et al., 2006). Such approaches can be easily and efficiently implemented, especially with a parallel computer (Pan et al., 2004). Thus the pseudo-potential Lattice Boltzmann approach seems, to date, to be the most convenient method for performing multiphase flow simulations in virtual wood samples.

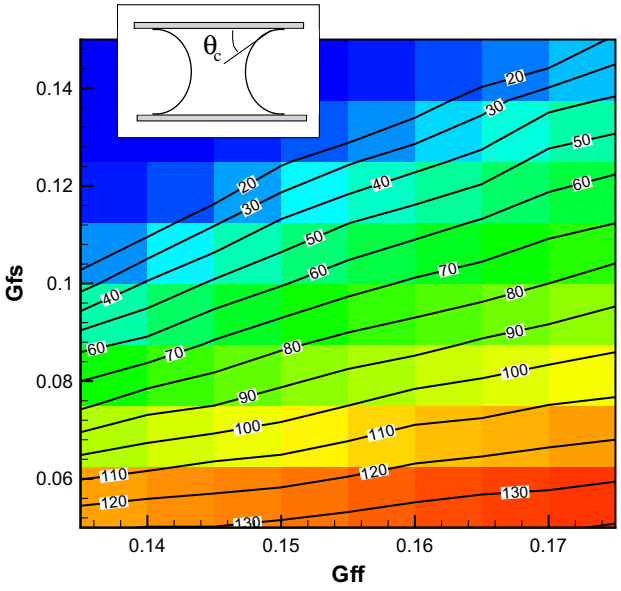

Fig. 6. Values of contact angle θ_c as a function of both G^{FF} (abscissa) and G^{FS} (ordinate).

4. Capillary invasion of a wood sample

4.1. Numerical setup

The purpose of the present work was to study the purely capillary invasion of a wood sample. It was therefore crucial to eliminate artificial effects on imbibition phenomena, especially within the liquid bath. We did this by following the method proposed by Chibbaro et al. (2009) to simulate an infinite liquid bath. We defined $\vec{e}_z$ as the imbibition direction, and n_z as the size, in $\vec{e}_z$ direction, of the grid which defined the sample anatomy. We assumed that $n_z' = 2n_z$ was the size of the effective simulation box in the $\vec{e}_z$ direction. The wood sample was placed between planes $z = n_z + 1$ and $z = n_z'$, and the nodes between planes $z = 1$ and $z = n_z$ were assumed to be fluid nodes. Periodic boundary conditions were assumed throughout. First, a liquid layer was placed in the simulation box without any solid node. This initial layer was placed between planes $z = 20$ and $z = n_z + 20$, the initial value of $\vec{u}$ was fixed at $\vec{u} = \vec{0}$, the initial values of f_i^{eq} were deduced from fields ρ and $\vec{u}$, and the initial values of f_i were set at f_i^{eq}.

At this point, the system is simulated through 20,000 iterations to ensure equilibrium. In a second step, the solid nodes are introduced, and the capillary imbibition starts and is computed until 250,000 iterations. The numerical setup is summarized in Fig. 7.

Both distances and time are expressed in lattice units, as grid step and time step are fixed to the unit. Therefore, in LB, the effect of time step cannot be analysed separately from the grid space. If the grid space is modified, a scaling in space and in time should be performed to compare the results. This point was checked on a simple configuration: we performed a simulation of capillary imbibition of an ideal bifurcation and two grid sizes ($n_x = 35$, $n_y = 35$ and $n_z = 350$ and $n_x = 50$, $n_y = 50$ and $n_z = 500$). From the

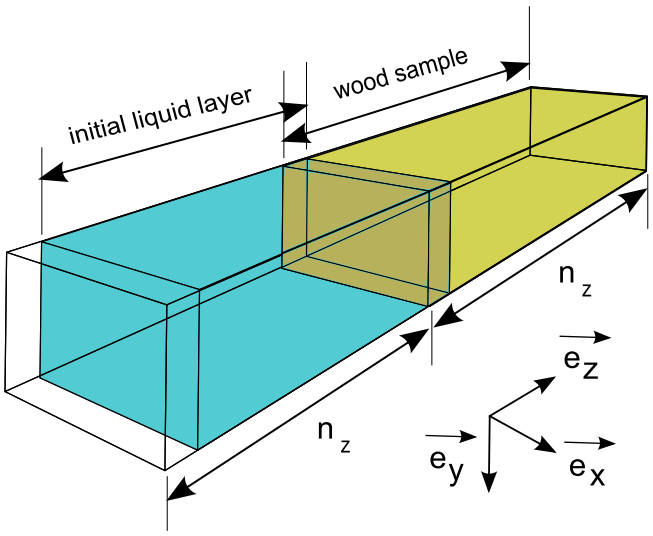

Fig. 7. Numerical setup for purely capillary imbibition of a porous medium.

computed results, we extracted rising curves in both sub-vessel 1 and sub-vessel 2 just in the same way. We observed the same behavior in the smaller grid and in the larger one. A curve crossing point at height z_c could be identified, and z_c/n_z has the same value in both cases. As a conclusion, we can say that results are grid-independent, provided the change in grid size is not sufficient to significantly change the grid Reynolds's number.

4.2. Results

Numerical experiments on capillary imbibition were carried out on the virtual birch sample anatomy described earlier (Fig. 4). The previously described simulation process was followed. We used the values $G^{FF} = 0.14$ and $G^{FS} = 0.08$ to impose a wetting solid phase. System dimensions were $n_x = 71$, $n_y = 133$, $n_z = 717$ and $n_{z'} = 1434$ which produces a numerical box with more than 6×10^6 lattices nodes. Using 64 processor cores of our Infiniband-based cluster, a typical run requires approximately 40 h to perform 250,000 iterations.

As can be seen in Fig. 8, the liquid/vapor interfaces exhibit menisci and, as expected, the liquid phase invades the vascular system, driven by wetting forces. Whereas imbibition within vessels 1–3 is a relatively common phenomenon as it occurs in channels close to cylindrical tubes, the case of vessel 4 is very interesting. When the liquid phase reaches the first bifurcation, the propagation interface is split into two menisci (Fig. 8:t = 90,000). After this step, the imbibition velocities within vessels 4a and 4b are different. Capillary invasion is slower in the larger vessel (4b) than in the narrower one (4a) (Fig. 8: t = 140,000). Then, when the liquid phase in vessel (4a) reaches the second bifurcation, its further propagation is stopped until vessel (4b) has been fully invaded. At this step, the 4a and 4b menisci coalesce and imbibition of the

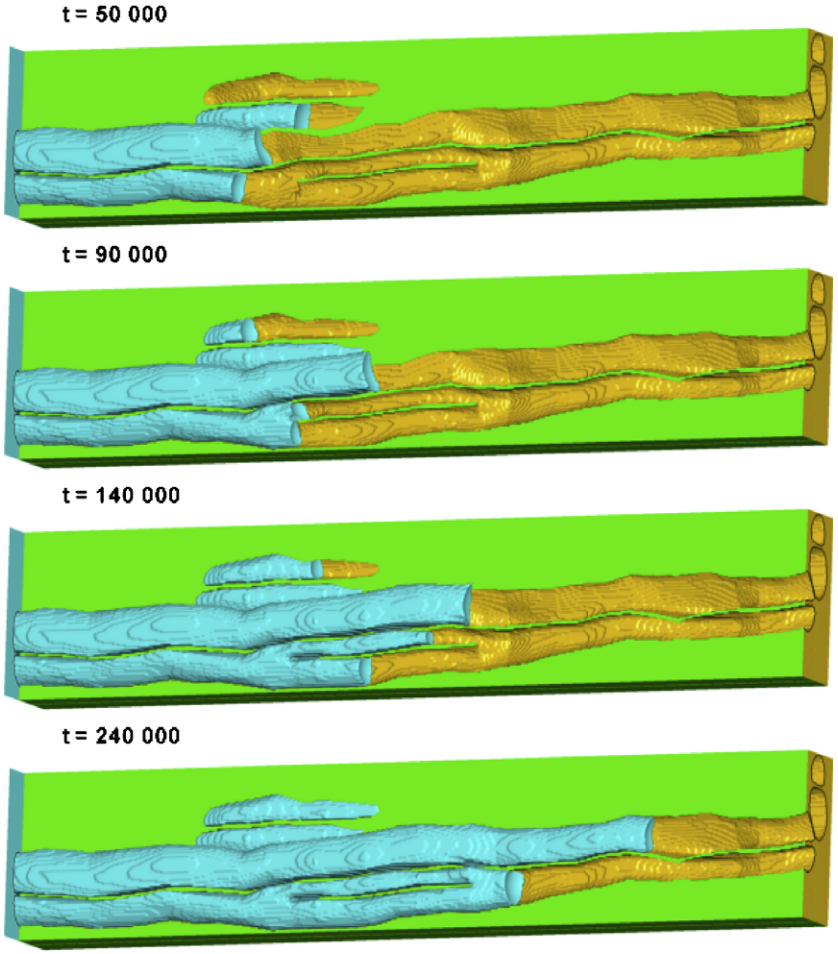

Fig. 8. Capillary invasion of the birch sample for different time values (lattice units). The dates were chosen to emphasize splitting of the meniscus in vessel 4 (t = 90,000) and coalescence of the resulting liquid columns (t = 240,000).

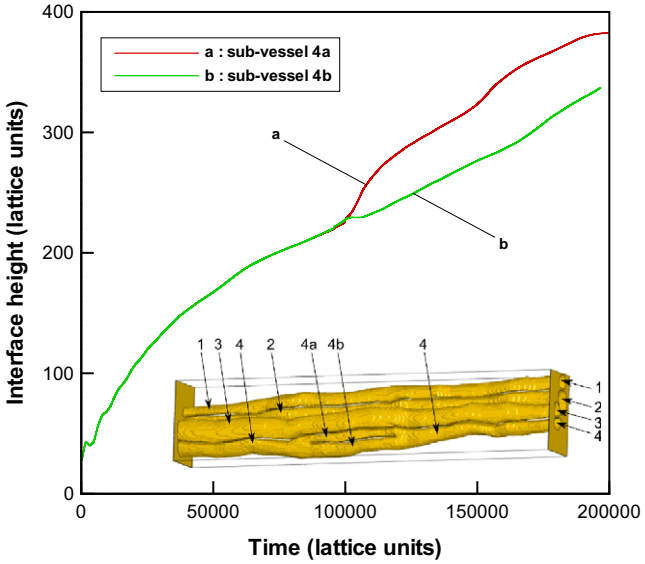

Fig. 9. Height of menisci in both 4a and 4b vessels as a function of time. A view of vascular anatomy (Fig. 4) is included.

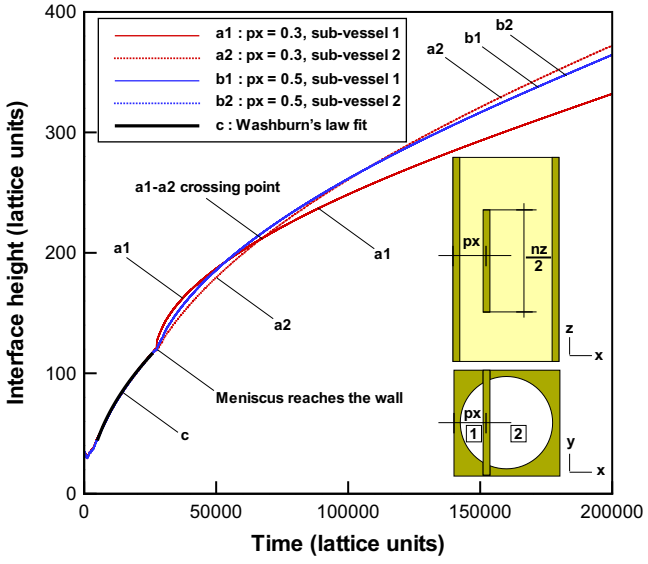

Fig. 10. Ideal bifurcation within a cylindrical tube: results.

upper part of vessel 4 can continue in the same way as in the other vessels (Fig. 8:$t = 240{,}000$). To confirm these phenomena, we tracked the liquid–vapor interface throughout the simulation:

The interface was traced inside both the 4 – 4a – 4 vessel path and the 4 – 4b – 4 vessel path. The density value ρ was extracted along a polyline defined by contour barycenters, as computed by *MeshPore* 3D, and the meniscus position was defined by curvilinear abscissa where the value $\rho = \frac{(\rho_L+\rho_V)}{2}$. As can be seen in Fig. 9, when the first bifurcation is reached, capillary invasion in the 4a sub-vessel becomes faster than in the 4b sub-vessel.

5. Discussion

It is well-known that, in the absence of gravity, capillary imbibition of a tube is dominated by a mechanism of competition between capillary forces and viscous forces (Chibbaro et al., 2009). In the simple case of a cylindrical tube, the assumption that inertia is negligible after a very short transitory period leads to Washburn's law (Washburn, 1921):

$$h^2 = \frac{\sigma d \cos\theta_c}{4\eta} t \tag{18}$$

where h is the height of the liquid phase inside the tube, d is the tube diameter, η is the viscosity of the fluid, and θ_c is the contact angle at the liquid/solid/gas triple line. Queries arise when the Eq. (18) is compared with the simulation results. According to Washburn's law, the speed of capillary invasion should increase with tube diameter. However, in our simulation, the behavior of the liquid phase after the bifurcation (Fig. 8) was in contradiction with this law.

We addressed this point by performing numerical experiments with an ideal bifurcation. We defined the solid phase as a cylindrical tube in which a flat longitudinal wall was inserted (Fig. 10: inset). The wall was inserted in a yz plane, the position of the wall was defined as p_x and the width was $n_x/10$. The fluid–fluid interaction parameters were fixed at $G^{FF} = 0.14$, and the wetting properties of the wall were exactly the same as for the tube, the interaction parameters being $G^{FS} = 0.08$ for each solid node. The same approach, as before, was applied to define the system dimensions and simulation procedure, (Fig. 7) and to set the following parameters at $n_x = 50$, $n_y = 50$, $n_z = 500$, and, as a consequence, $n'_z = 1000$. Two different cases were tested: case a:$p_x = n_x/3$ and case b:$p_x = n_x/2$. The height of the liquid–vapor interface within sub-vessels 1 and 2 was recorded and the computed results are shown in following figure:

The first stage of imbibition involves the classical capillary invasion of a cylindrical tube, and obeys Washburn's law (Fig. 10: curve c). All the curves are superimposed at this stage, as the tube diameter is the same for both numerical simulations. When the meniscus reaches the wall (Fig. 10: first annotation), the subsequent behavior depends on p_x. In the case of equal-sized sub-vessels ($p_x = n_x/2$), the curves of sub-vessel 1 and sub-vessel 2 remain superimposed until the last iteration (Fig. 10: curves $b1$ and $b2$) because the imbibition velocity is the same in both sub-vessels. It can be seen that imbibition briefly accelerates just after splitting of the meniscus. It is clear that new solid nodes increase the driving forces whereas narrower vessels increase viscous dissipation. Washburn's law is a consequence of the competition between these contradictory effects. However, when the initial meniscus reaches the transverse wall, a transitory regime takes over, in which the meniscus (capillary forces) is of small hydraulic diameter while the flow (viscous forces) still occurs in a large diameter. The other test case ($p_x = n_x/3$) provides information about the influence of the relative widths of the sub-vessels. As can be seen on curves $a1$ and $a2$ in Fig. 10, the imbibition velocities are identical until the meniscus reaches the wall, but exhibit different patterns after this step. As explained previously, the acceleration is greater in the narrow sub-vessels than in the larger single vessel. During this transient stage, in the same way as in the real bifurcation within the virtual birch sample (Fig. 8: $t = 140{,}000$), Washbrun's law no longer holds. Later in the simulation, the height of sub-vessel 2 exceeds the height of sub-vessel 1 (Fig. 10: second annotation): the viscous forces and the capillary forces are again expressed in the same diameter, so that Washburn's law applies again.

These results provide a clear interpretation of the counter-intuitive evolution previously observed in the virtual birch sample. When the liquid phase reaches the first bifurcation of the 4th vessel, the velocity inside the 4th (a) sub-vessel increases strongly as the transitory regime takes place. However, the long-term behavior is not observed in this case, as the liquid column in the 4th (b) sub-vessel coalesces with the liquid column in the 4th (a) sub-vessel before this long-term behavior can occur. Consequently, only the transitory regime would be observed in our case of wood morphology.

6. Conclusion

In this paper, we have proposed a systematic approach for simulating multiphase flows in the vascular system of wood. Sample anatomy was determined from successive microtome sections and microscope images. The *Meshpore* software was applied to generate the contours of vessels in a vectorial way, suitable for 3D interpolation and lattice generation of any resolution. Intermediate slices were generated between real sections using an interpolation scheme to improve resolution in the longitudinal direction and 2D grids of points were deduced from the final set of slices. The resulting anatomy was a 3D cubic lattice, which provided solid boundaries for a Shan–Chen type Lattice Boltzmann scheme.

This framework was then used to simulate capillary invasion by means of a customized parallel numeric code, *FlowPore*. Special attention was given to phenomena occurring when a meniscus reached a bifurcation, i.e. where a vessel split into two sub-vessels. The observed imbibition in the narrower vessel was faster than in the larger one, and in contradiction with Washburn's law. Numerical experiments, involving an ideal bifurcation in a cylindrical tube, clearly proved that this behavior was transitory, and that it occurred near the bifurcation where the capillary forces and viscous forces were not expressed in the same hydraulic diameter.

In the future, this chain of tools could be applied to study the vascular system of different plants. For this purpose, micro-tomography is certainly a better solution than our tedious method to collect the 3-D morphology. The experimental validation is also a crucial concern. The challenge here is the ability of a 3-D imaging system to be fast enough to follow the water menisci during capillary invasion: NMR imaging or ultra-fast tomography are possible candidates.

Acknowledgements

The authors gratefully acknowledge the financial support of the CPER 2007–2013 "Structuration du Pole de Competitivite Fibres Grand Est" (Competitiveness Fibre Cluster), through local (Conseil General des Vosges), regional (Region Lorraine), national (DRRT and FNADT) and European (FEDER) funds.

References

Agoua, E., Zohoun, S., Perré, P., 2001. Utilisation d'une double enceinte pour déterminer la diffusivité massique du bois en régime transitoire: recours à la simulation numérique pour valider la méthode d'identification. Int. J. Heat Mass Transfer 44, 3731–3744.

Almeida, G., Leclerc, S., Perré, P., 2008. NMR imaging of fluid pathways during drainage of softwood in a pressure membrane chamber. Int. J. Multiphase Flow 34, 312–321.

Aumann, A., Ford, E.D., 2002. Parameterizing a model of douglas fir water flow using a tracheid-level model. J. Theor. Biol. 219, 431–462.

Chibbaro, S., Biferale, L., Diotallevi, F., Succi, S., 2009. Capillary filling for multicomponent fluid using the pseudo-potential lattice Boltzmann method. Proceedings for DSFD 2007. Eur. Phys. J. Special Topics 171, 223–228.

Comstock, G.L., 1970. Directional permeability of softwoods. Wood Fiber Sci. 1, 283–289.

De Sousa, F.S., Mangiavacch, N., Nonato, L.G., Castelo, A., Tomé, M.F., Ferreira, V.G., Cuminato, J.A., Mc Kee, S., 2004. A front-tracking/front-capturing method for the simulation of 3D multi-fluid flows with free surfaces. J. Comput. Phys. 198, 469–499.

Dullien, F., 1992. Porous Media: Fluid Transport and Pore Structure. Academic Press, San Diego.

Frank, X., Perré, P., 2010. The potential of meshless methods to address physical and mechanical phenomena involved during drying at the pore level. Drying Technol. J. 28, in press.

Gunstensen, A.K., Rothman, D.H., Zaleski, S., Zanetti, G., 1991. Lattice Boltzmann model of immiscible fluids. Phys. Rev. A 43, 4320–4327.

Hacke, U., Sperry, J., Pitterman, J., 2004. Analysis of circular bordered pit function – II. Gymnosperm tracheids with torus-margo pit membranes. Am. J. Botany 91, 386–400.

Hardy, J., de Pazzis, O., Pomeau, Y., 1976. Molecular dynamics of a lattice gas: transport properties and time correlation functions. Phys. Rev. A 13, 1949–1961.

Hatiboglu, C.U., Babadagli, T., 2008. Pore-scale studies of spontaneous imbibition into oil-saturated porous media. Phys. Rev. E 77, 066311.

He, X., Chen, S., Zhang, R., 1999. A lattice Boltzmann scheme for incompressible multiphase flow and its application in simulation of Rayleigh–Taylor instability. J. Comput. Phys. 152, 642–663.

Henrich, B., Cupelli, C., Moseler, M., Santer, M., 2007. An adhesive DPD wall model for dynamic wetting. Europhys. Lett. 80, 60004.

Inamuro, T., Ogata, T., Tajima, S., Konishi, N., 2004. A lattice Boltzmann method for incompressible two-phase flows with large density differences. J. Comput. Phys. 198, 628–644.

Kwon, G.H., Chae, S.W., Lee, K.J., 2003. Automatic generation of tetrahedral meshes from medical images. Comput. Struct. 81, 765–775.

Lee, T., Lin, C.L., 2005. A stable discretization of the lattice Boltzmann equation for simulation of incompressible two-phase flows at high density ratio. J. Comput. Phys. 206, 16–47.

Martys, N.S., Chen, H., 1996. Simulation of multicomponent fluids in complex three dimensional geometries by the lattice Boltzmann method. Phys. Rev. E 53, 743–750.

Pan, C., Prins, J.F., Miller, C.T., 2004. A high-performance lattice Boltzmann implementation to model flow in porous media. Comput. Phys. Commun. 158, 89–105.

Panshin, A., de Zeeuw, C., 1980. Textbook of Wood Technology: Structure, Identification, Properties and Uses of the Commercial Woods of the United States and Canada, forth ed. McGraw-Hill, New York.

Perré, P., Turner, I., 2001. Determination of the material property variations across the growth ring of softwood for use in a heterogeneous drying model. Part I: capillary pressure, tracheid model and absolute permeability. Holzforchung 55, 318–323.

Perré, P., Karimi, A., 2002. Fluid migration in two species of beech (Fagus silvatica and Fagus orientalis): a percolation model able to account for macroscopic measurements and anatomical observations. Maderas. Cienc. y tecnol. 4, 50–68.

Perré, P., 2005. MeshPore: a software able to apply image-based meshing techniques to anisotropic and heterogeneous porous media. Drying Technol. J. 23, 1993–2006.

Raiskinmäki, P., Shakib-Manesh, A., Jäsberg, A., Koponen, A., Merikoski, J., Timonen, J., 2002. Lattice-Boltzmann simulation of capillary rise dynamics. J. Stat. Phys. 107, 143–158.

Sbragaglia, M., Benzi, R., Biferale, L., Succi, S., Toschi, F., 2006. Surface roughness-hydrophobicity coupling in microchannel and nanochannel flows. Phys. Rev. Lett. 97, 204503.

Shan, X., Chen, H., 1993. Lattice Boltzmann model for simulating flows with multiple phases and components. Phys. Rev. E 47, 1815–1820.

Siau, J.F., 1984. Transport Processes in Wood. Springer-Verlag, Berlin.

Štěpánek, F., Rajniak, P., 2006. Droplet morphologies on particles with macroscopic surface roughness. Langmuir 22, 917–923.

Steppe, K., Cnudde, V., Girard, C., Lemeur, R., Cnudde, J., Jacobs, P., 2004. Use of X-ray computed microtomography for non-invasive determination of wood anatomical characteristics. J. Struct. Biol. 148, 11–21.

Succi, S., 2001. The Lattice Boltzmann Equation for Fluid Dynamics and Beyond. Clarendon Press, Oxford.

Sukop, M.C., Or, D., 2004. Lattice Boltzmann method for modeling liquid–vapor interface configurations in porous media. Water Resour. Res. 40, W01509.

Sukop, M.C., Huang, H., Lin, C.L., Deo, M.D., Oh, K., Miller, J.D., 2008. Distribution of multiphase fluids in porous media: comparison between lattice Boltzmann modeling and micro-X-ray tomography. Phys. Rev. E 77, 026710.

Swift, M.R., Osborn, W.R., Yeomans, J.M., 1995. Lattice Boltzmann simulation of nonideal fluid. Phys. Rev. Lett. 75, 830–833.

Swift, M.R., Orlandini, E., Osborn, W.R., Yeomans, J.M., 1996. Lattice Boltzmann simulations of liquid–gas and binary fluid systems. Phys. Rev. E 54, 5041–5052.

Tanguy, S., Berlemont, A., 2005. Application of a level set method for simulation of droplet collisions. Int. J. Multiphase Flow 31, 1015–1035.

Tartakovsky, A.M., Ward, A.L., Meakin, P., 2007. Pore-scale simulations of drainage of heterogeneous and anisotropic porous media. Phys. Fluids 19, 103301.

Trtik, P., Dual, J., Keunecke, D., Mannes, D., Niemz, P., Stähli, P., Groso, A., Stampanoni, M., 2007. 3D imaging of microstructure of spruce wood. J. Struct. Biol. 159, 45–55.

Tyszka, J.M., Fraser, S.E., Jacobs, R.E., 2005. Magnetic resonance microscopy: recent advances and applications. Current Opin. Biotech. 16, 93–99.

Valli, A., Koponen, A., Vesala, T., Timonen, J., 2002. Simulations of water flow through bordered pits of conifer xylem. J. Statist. Phys. 107, 121–142.

Vogel, H.J., Tölke, J., Schulz, V.P., Krafczyk, M., Roth, K., 2005. Comparison of a lattice-Boltzmann model, a full-morphology model, and a pore network model for determining capillary pressure–saturation relationships. Vadose Zone J. 4, 380–388.

Washburn, E.W., 1921. The dynamics of capillary flow. Phys. Rev. E 17, 273–283.

Yu, Z., Hemminger, O., Fan, L.S., 2007. Experiment and lattice Boltzmann simulation of two-phase gas–liquid flows in microchannels. Chem. Eng. Sci. 62, 7172–7183.

Yuan, P., Schaefer, L., 2006. A thermal lattice Boltzmann two-phase flow model and its application to heat transfer problems, part 1. Theoretical foundation. J. Fluids Eng. 128, 142–150.

Zimmermann, M.H., 1983. The Ascent of Sap in Trees. Springer-Verlag, Berlin.